AIAA JOURNAL
Vol. 34, No. 2, February 1996

Experimental Investigation of Supersonic Gaseous Injection into a Supersonic Freestream

Gregory J. McCann* and Rodney D. W. Bowersox†
U.S. Air Force Institute of Technology, Wright–Patterson Air Force Base, Ohio 45433–7765

An experimental study of the mean and turbulent flowfield associated with low-angled supersonic gaseous injection into a supersonic freestream was performed. Air was injected at Mach 1.8, with an effective back pressure ratio of 3.0, through an orifice at an angle of 25 deg into a Mach 2.9 air freestream ($Re/m = 15 \times 10^6$). Cross-film anemometry and conventional mean flow probe surveys were acquired across the plume at two downstream stations ($x/d = 20$ and 40). Schlieren photography was used for qualitative flow visualization. Turbulence measurements included contours of the turbulent kinetic energy and the full compressible Reynolds shear stresses in both the x–y and x–z planes. Mean flow data included Mach number, three-dimensional velocity components, and vorticity. The measurements indicated that the mean and turbulent flow structure of the injection plume were strongly influenced by the presence of a counter-rotating vortex pair ($|\omega_x|_{max} \approx 15{,}000$ /s). The turbulent kinetic energy was found to have two peaks colocated with the vortices. The turbulent shear stress distributions across the plume were found to be highly three dimensional and complicated by both the additional strain rates associated with the vorticity and turbulent convection. The present results also implied that the compressibility terms in the Reynolds shear stress accounted for about 67.0–75.0% of the total shear stress level, i.e., $\bar{u}\overline{\rho' v'}/\bar{\rho}\overline{u' v'}$ and $\bar{u}\overline{\rho' w'}/\bar{\rho}\overline{u' w'}$ were in the range of 2.0–3.0.

Nomenclature

d	= injector exit diameter
k	= turbulent kinetic energy
M	= Mach number
Nu	= Nusselt number
p	= pressure
Re	= Reynolds number
T	= temperature
u, v, w	= velocity components
x, y, z	= Cartesian coordinates
α	= $[1 + 0.5(\gamma - 1)M^2]^{-1}$
γ	= ratio of specific heats
θ	= injection angle
μ	= viscosity
ρ	= density
τ	= shear stress

Subscripts

c	= compressible
e	= effective
t	= total condition
∞	= freestream condition

Superscripts

T	= turbulent
$'$	= fluctuating component
$-$	= mean component

Introduction

LOW-ANGLED gaseous injection into a supersonic freestream appears in many practical situations. One current interest is fuel injection into a supersonic combustion ramjet (Scramjet) engine. As discussed in Fuller et al.[1] and Mays et al.,[2] residence times for the fuel in a supersonic combustion chamber would be on the order of milliseconds. Hence, turbulent mixing is of paramount importance. In addition, as the vehicle flight speed continues to increase, the net propulsive thrust becomes a smaller fraction of the gross airstream entering and leaving the engine, and thus total pressure loss is also a critical concern. Parametric studies on injection angle, ranging from normal injection to that of a downstream facing slot, have been performed.[3,4] Other feasible uses include re-entry cooling, thrust vector control, and stall suppression.

Because of the complicated flow physics, low-angled supersonic injection into a supersonic freestream is currently intractable from an analytical perspective and also challenging from an experimental or computational viewpoint. Three of the formidable flow difficulties include three-dimensionality, compressibility, and turbulence.

Although not the only limitation, turbulence modeling remains a controlling factor in the accuracy of all high-speed, high Reynolds number numerical Navier–Stokes predictions. Since the computational resources necessary to directly simulate, or perform a large eddy simulation of, high Reynolds number turbulent flows, for all but the simplest of geometries, are not currently available, engineers must rely on an averaged approximate form of the Navier–Stokes equations. The two common approaches are Reynolds time and Favre mass-weighted time averaging. In either case, turbulence models are necessary to close the system.

Turbulence modeling issues associated with supersonic injection into a supersonic freestream are particularly challenging. Historically, turbulent flows have been categorized for which appropriate closure formulations have been developed. For example, two well-established classifications are wall boundary and free shear layers. Gaseous injection into a cross stream includes features from both wall bounded and free shear layers, as well as an interaction between the two. In addition, the effects of compressibility on turbulent flows remain unclear. However, for high-speed, two-dimensional, planar coflowing cases, the effects of compressibility on the spreading rate[5] and the turbulent field[6] have been documented.

Studies of supersonic, three-dimensional, injection flows that include both turbulent and mean flow measurements are scarce. Presented here are results from an experimental study aimed at providing detailed information about the structure of the mean and turbulent flow associated with supersonic gaseous injection into a supersonic freestream. Conventional mean flow methods along with hot-film thermal anemometry[7] were used to obtain contours of Mach number, three-dimensional velocity components, vorticity,

Received April 11, 1995; revision received Aug. 31, 1995; accepted for publication Sept. 23, 1995. This paper is declared a work of the U.S. Government and is not subject to copyright protection in the United States.

*Graduate Research Assistant, Department of Aeronautics and Astronautics. Member AIAA.

†Assistant Professor, Department of Aeronautics and Astronautics. Member AIAA.

Reynolds shear stress components, and the turbulent kinetic energy across the plume.

Experimental Apparatus

Facilities

All tests were performed in the Air Force Institute of Technology supersonic wind tunnel. This blowdown, pressure-vacuum system provided 25-s test times at Mach 2.9. The Mach number variation across the tunnel has been documented as ±0.03. The freestream turbulent kinetic energy across the tunnel has also been documented as nominally 30.0 m^2/s^2, which is about 0.008% of the freestream kinetic energy per unit mass. The settling chamber pressure and temperature were maintained at 2.0 ± 0.03 atm and 294 ± 2 K for all tests. The freestream Reynolds number per meter was 15.0×10^6. The test section was 6.35 × 6.35 cm in cross section and 28.0 cm long. The tunnel flow conditions are summarized in Table 1.

The injector model was built into the ceiling of the tunnel as shown on the schematic in Fig. 1; also shown is the right-hand coordinate system. The injector Mach number, based on area ratio, was designed to be 1.8. This value was confirmed in a bench top test (the pitot pressure ratio was measured as 0.8). The divergence angle of the axisymmetric conical nozzle was 0.83 deg. The injector throat diameter was 3.22 mm, and the exit diameter was 3.86 mm. The injection angle was 25 deg relative to the freestream. Since the injector was at an angle, the exit port was elliptical with a 3.86 and 9.14 mm minor and major axis length, respectively. The exit diameter normal to the axial flow direction was taken to be the minor axis length. To compare the results qualitatively with other data in the literature, the effective back pressure was modeled as the pressure that would occur on the surface of an axisymmetric cone with a half-angle equal to that of the injection angle.[1] For the present study, the jet total pressure was set at 4.0 ± 0.08 atm. Thus, the jet exit pressure ratio p_j/p_{eb} was equal to 3.0. The injectant gas was chosen to be air. The jet air was tapped from the tunnel source; hence the injectant total temperature was also 294 K. The jet exit conditions are also included in Table 1.

Instrumentation and Data Analysis

Microsecond spark schlierens were taken. Conventional pitot and cone-static pressure contours across the plume at both measurement stations, $x/d = 20$ and 40, were acquired. The pitot pressure probe was constructed from 1.59-mm outer diameter stainless steel tubing. The end of the probe was crimped such that the height of the opening was approximately half of the width. The cone-static probe was machined from stainless steel. The semivertex angle was measured as 10 ± 0.03 deg. Four pressure taps were located at 90 deg intervals around the circumference of the probe. This configuration allowed for probe misalignment errors of ±6.0–7.0 deg to be canceled.[8] The diameter of the probe at the location of the four pressure taps was 1.7 mm. The Mach number was computed from the ratio of the cone-static and pitot pressure data using Taylor–Mccoll conical flow theory and the Rayleigh–Pitot formula. A random error analysis indicated a ±3.0% uncertainty in the Mach number results.

Table 1 Summary of freestream and injection parameters

	Mach	u, m/s	p, kPa	ρ, kg/m^3	Re/m, × 10^6	k, m^2/s^2
Freestream	2.9	609.0	6.41	0.204	15.0	30.0
Injector	1.8	482.0	67.2	1.32	53.0	NA[a]

[a]NA = not available.

TSI model IFA 100 constant temperature anemometer systems were used with TSI 1243-20 cross-film probes.[9] The platinum hot-film probes has cylindrical sensors, which were 1.0 mm in length and 51 μm in diameter. The cross-film probe total cross-sectional area was nominally 1.0 mm^2. Measurements were obtained in both the x–y and x–z planes. Probe alignment was maintained to within ±1.0 deg. The frequency response was optimized to nominally 150 kHz by the square wave technique in the Mach 2.9 freestream. The majority of the data were taken using the single overheat technique,[7] where the wire resistance ratio was set to 2.03 ± 0.03. Multiple overheat[7] data were also acquired along the centerline of the jet plume. For that data, eight resistance overheat ratios, in the range of 1.3–2.1, were used over a series of eight runs. The sampling rate was 20 kHz, and 2048 samples were averaged into a single data point.

The cross-film data reduction techniques used here stemmed from the pioneering work of Kovasznay[10] and Spangenberg.[11] In general, the reduction was based on the empirical heat loss formula

$$Nu = a\sqrt{Re_e} + b$$

where Re_e is the effective cooling Reynolds number,[6,7] which is based on the wire diameter. The cosine law as demonstrated by Spangenberg[11] was assumed valid. In addition, the flow angles in the present thin layer type flow were not expected to be very large (on the order of ±10 deg relative to the freestream). The probes were calibrated at each overheat ratio by placing them in the freestream and varying the tunnel total pressure. Since a single contour involved a series of runs, the probes were intermittently calibrated throughout the testing to ensure that they had not suffered from oxidation or contamination. The present study found that the minimum linear regression correlation coefficient for the preceding heat transfer law was 0.99.

The multiple overheat data were reduced using the generalized least-squares method.[7] In summary, multiple overheat cross-wire anemometry provides the mean mass flux ρu_i; the mean total temperature $\bar{T}_t$; the mass flux components and total temperature fluctuation turbulence intensities, $\sqrt{(\rho u_i)'^2}$ and $\sqrt{(\overline{T_t'^2})}$, respectively; and

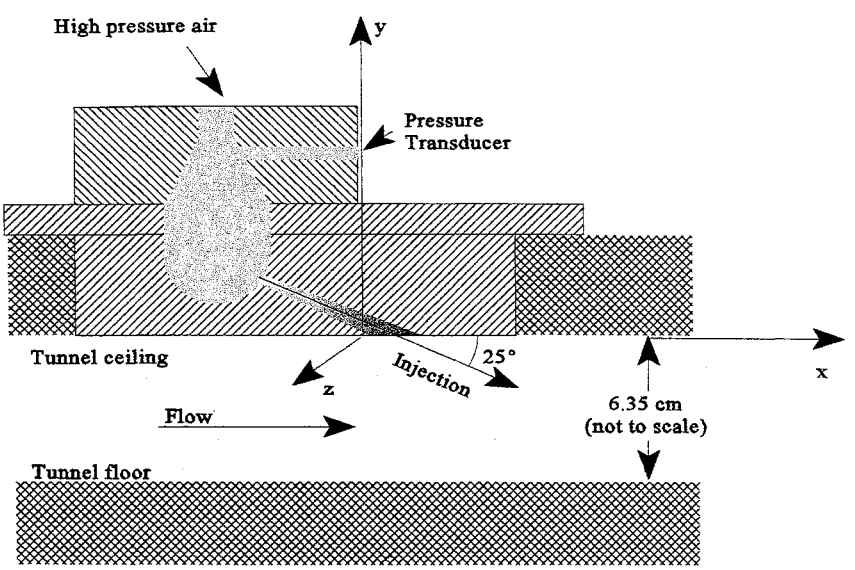

Fig. 1 Schematic of injector and test section.

the $\overline{(\rho u_i)'(\rho u_j)'}$ and $\overline{(\rho u_i)'T_t'}$ correlations. A random error analysis indicated a 5.0 and 10.0% uncertainty in the turbulence intensity and correlation results, respectively.

For the single overheat technique, the mean total temperature was assumed constant, and the total temperature fluctuations were neglected. The results discussed later confirm the validity of the single overheat technique for the present adiabatic flow.

The compressible Reynolds shear stress

$$\tau_{ij}^T = -\bar{\rho}\overline{u_i'u_j'} - \bar{u}_i\overline{\rho'u_j'} - \bar{u}_j\overline{\rho'u_i'} \tag{1}$$

can be related to the cross-wire turbulence data as follows[6]:

$$\tau_{ij}^T = -\frac{\overline{(\rho u_i)'(\rho u_j)'}}{\bar{\rho}} + \bar{\rho}\bar{u}_i\bar{u}_j\overline{\left(\frac{\rho'}{\bar{\rho}}\right)^2} \tag{2}$$

where the first term on the right-hand side is directly measurable. The second term can be estimated by uncoupling the cross-wire turbulence results.[6,7] An important attribute of Eq. (2) is that for thin layer type flows, where the transverse or span velocity is generally very small, the second term on the right-hand side is usually much smaller than the first. Thus, direct measurement of the full compressible Reynolds turbulent shear stress [i.e., the summation of the three terms on the right-hand side of Eq. (1)] is possible. In the present study, the relative magnitude of the two terms on the right-hand side of Eq. (2) was compared by applying an uncoupling procedure, which is discussed later.

Uncoupling the cross-wire results allowed for all of the Reynolds shear stress terms in Eq. (1) to be inferred. This procedure involved assuming that the product $\alpha(p'/\bar{p})$ is much smaller than both $(\rho u)'/\overline{\rho u}$ and $\rho'/\bar{\rho}$, where $\alpha = \bar{T}/\bar{T}_t$. For the present flow, α was in the range of 0.3–0.5; thus, even if the pressure fluctuations were not zero, perhaps, due to being multiplied by α, their effects on the cross-wire response were still small. Kistler[12] suggested that p' was second order and hence neglected it for wall boundary layers up to Mach 4.7. Also, Bowersox and Schetz,[6] studying a Mach 4.0 free mixing layer, demonstrated that the density fluctuation turbulence intensity estimated from cross-wire anemometry, where the pressure fluctuations were neglected, was in very good agreement (±5%) with optical measurements.

Results

Flow Visualization

Six hundred nanosecond (0.6 μs) exposure time schlieren photographs were taken. Shown in Fig. 2 is a schlieren of the injector region, where the knife edge was aligned with the flow, and the top half of the light was cut off. The injector was located in the tunnel ceiling, and the flow was from right to left. The salient features include the leading-edge shock due to the injection and a weaker recompression shock just downstream of the injector. The recompression shock was found to be unsteady as its position and shape varied over a series of photographs. The familiar lambda leading-edge shock structure is evident very near the upper wall, thus indicating a small separation bubble just upstream of the injector. The facility boundary layers and jet plume are also noticeable. The freestream boundary-layer thickness, δ_∞/d, just ahead of the injection was estimated from Fig. 2 as 1.6.

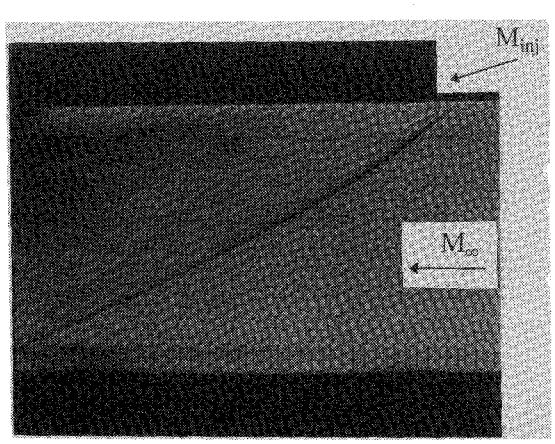

Fig. 2 Schlieren of injector region.

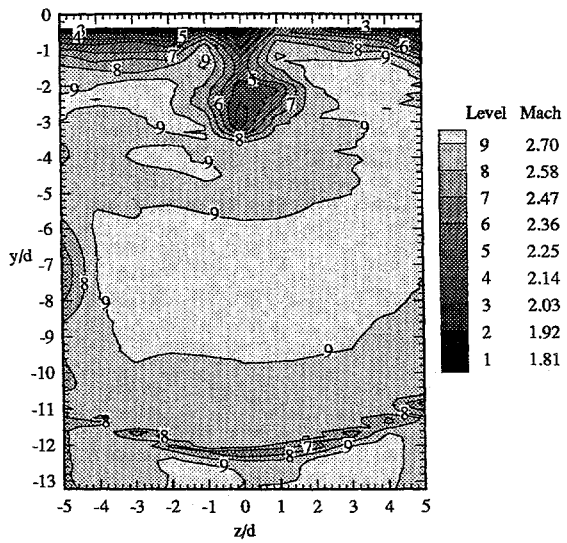

a) $x/d = 20$

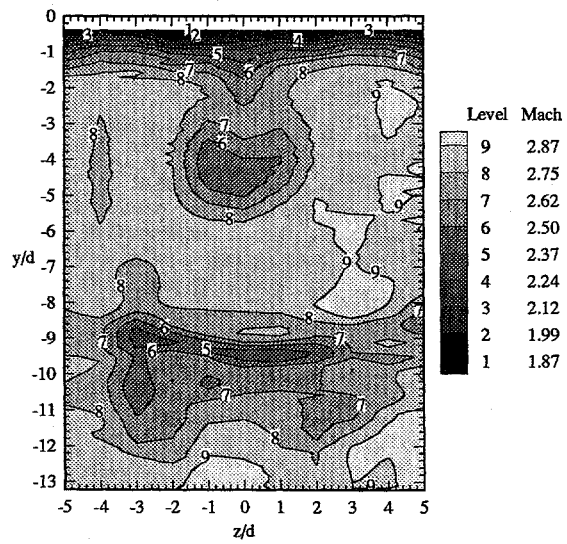

b) $x/d = 40$

Fig. 3 Mach number contours.

Mean Flow Measurements

The Mach number contours for $x/d = 20$ and 40 are shown in Fig. 3. The cross-film data, which are discussed later, indicated that at $x/d = 40$ the flow angle along the centerline of the plume was roughly −9.0 deg. At $z/d \approx \pm 2.0$, the flow angle was measured as 4.5 deg. Thus, the probe was inclined by −2.3 deg to minimize probe alignment errors. At $x/d = 20$, the magnitudes of the flow angles were found to be about 5.0 deg larger. Hence, the uncertainty of the $x/d = 20$ results are expected to be higher than the ±3.0% expected for the $x/d = 40$ station. The contours were oriented such that the flow was going into the page. The contours were constructed from a series of profiles acquired across the plume in intervals of $\Delta z = 1.0d$. All contours began at $y/d = -0.40$. The jet plume and wall boundary layer are clearly visible. Based on visual interpretation of Fig. 3, the plume at $x/d = 30$ had grown to a diameter of roughly $3.0d$. Also by this station, the plume center penetrated to approximately $-3.0d$. Also, the curved injector shock is clearly noticeable near the bottom of the contour. By the $x/d = 40$ station, the center of the plume penetrated to about $-4.5d$, and the

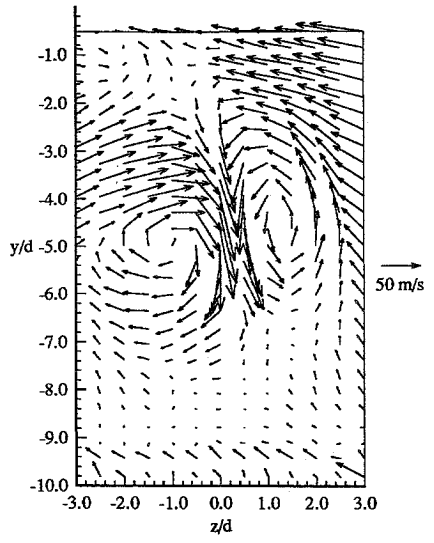

Fig. 4 y–z velocity vector contour (x/d = 40).

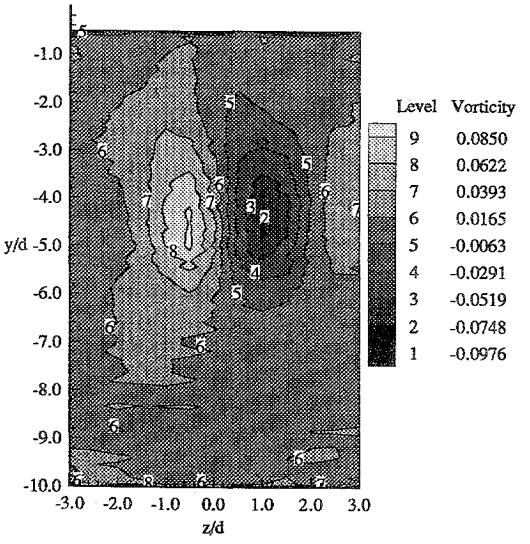

Fig. 5 x component of vorticity ($/(u_\infty/d)$, x/d = 40).

plume shape had become fuller, where the diameter had increased slightly to $4.0d$. If the center of the plume is assumed to be consistent with the location of maximum concentration, then the present measurements ($\rho u_j/\rho u_\infty = 5.11$) compare favorably with the helium injection results of Mays et al.[2] ($M_\infty = 3.0, \theta = 30$ deg, and $\rho u_j/\rho u_\infty = 2.2$), where they reported a penetration at $x/d = 40$ of also about $4.5d$.

The kidney[13] or horseshoe[14] shaped Mach number in the center of the plume was indicative of vortical motion within the jet plume. The Mach 6.0 concentration contours in Fuller et al.[1] also showed a similar shape. The nonuniform Mach number distribution near the bottom of the contour resulted from the injector leading-edge shock reflecting off the test section floor. Thus, the reflected leading-edge shock did not interact with the plume at $x/d = 40$. However, surface oilflow visualization indicated that the shock reflections off the side walls crossed the plume at $x/d \approx 30$.

Cross-film measurements were taken at the same two x/d locations. For these data, the spacing between profiles was decreased to $\Delta z = 0.5d$; however, the measurement field was reduced to just capture the plume. Again, the measurements started at $y/d = -0.40$. Only the results at the $x/d = 40$ station are presented as they are representative of the flow feature at both stations.

Shown in Fig. 4 is the y–z plane velocity vector contour. The expected probe alignment uncertainty indicated a ±10.0-m/s error bound for the present velocity measurements. Two counter-rotating vortices are clearly depicted in Fig. 4. The right or positive z side vortex was located slightly closer to the wall than the left vortex. Since the right vortex was closer to the wall, the entrained boundary-layer fluid from the right had a higher z component of momentum than that from the left vortex. Hence, the flow stagnated on the left side of the plume ($y/d = -2.0$ and $z/d = -1.0$). In addition, an apparent third vortex was just to the left and slightly above the stagnation point ($y/d = -1.5$ and $z/d = -2.5$).

A central finite difference was applied to the velocity data to estimate the x component of vorticity, i.e., $2\omega_x = (\partial\bar{w}/\partial y - \partial\bar{v}/\partial z)$. The results of that analysis are presented in Fig. 5. The peak magnitude $|\omega_x|_{\max}$ for each vortex was nominally 15,000 /s. There were several mechanisms that could have been responsible for inducing this secondary flow. First, in the initial injection region, as the crossflow wrapped around the jet, a lower pressure expansion along the back or downstream side of the jets would induce a rotational motion. Second, the turning of the jet flow into the crossflow direction would serve to generate or add energy to the secondary flow. This is somewhat analogous to the secondary flow rotation associated with flow in a curved duct. It is also possible that a nonuniform shearing around the periphery of the plume could have contributed to the rotational nature of the flow. The numerical study of Kim and Benson[15] for incompressible normal injection also predicted two downstream counter-rotating vortices.

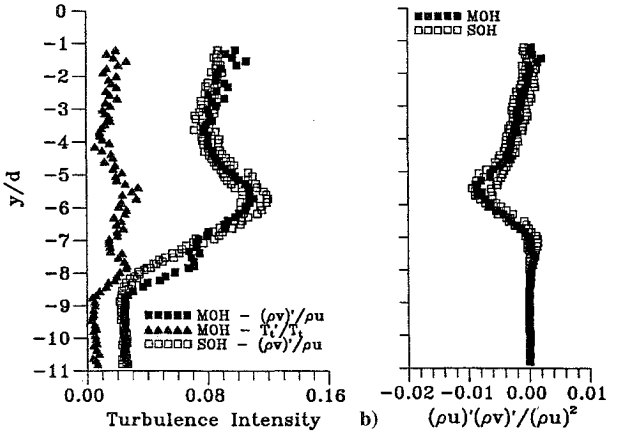

Fig. 6 Comparison of SOH and MOH x–y cross-film results (x/d = 40 and z/d = 0).

The structure of the mean flow and the ability of the flow to entrain freestream fluid are strongly affected by the strength of the vorticity. Hence, the presence and strength of the vortex pair are key factors in the effectiveness of the injectant gas mixing with the freestream flow as needed for scramjet fuel injection or to energize a boundary layer relevant to stall suppression. Based on the measured vorticity, the present flow experienced only a few revolutions by the $x/d = 40$ stations, which may indicate that the mixing enhancement due to the naturally occurring vorticity would not be very substantial. Although not measuring vorticity, recent studies[1,16] have attempted to augment mixing by enhancing the vortex generation through the use of yawed jets and jet arrays. In addition to experimental measurements, Cox et al.[16] also used computational techniques to evaluate the effectiveness of a new injector design. However, current numerical methods are hindered by the uncertainty associated with turbulence models, and the development of suitable closure formulations is inhibited by the lack of turbulence data.

Turbulent Flow Measurements

The majority of the present data were acquired using the single overheat technique. However, as mentioned earlier, to verify the approximations of that technique, multiple overheat data were acquired along the jet centerline. Compared in Fig. 6 are the single overheat (SOH, open symbols) and multiple overheat (MOH, closed symbols) turbulence intensity and shear stress results along the centerline of the plume. As can be seen, the agreement between the two methods is well within the experimental uncertainty. The single overheat results in Fig. 6 were acquired over separate runs; hence the scatter is indicative of the flow repeatability. The agreement between

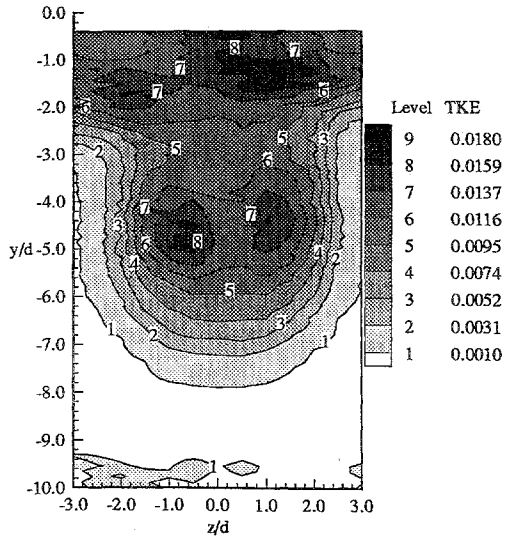

Fig. 7 Compressible turbulent kinetic energy/$\bar{u}^2$(x/d = 40).

the SOH and MOH results was not surprising since the total temperature turbulence intensity was only 0.02–0.03 across the plume. Hence, neglecting the total temperature fluctuations, as discussed earlier, was deemed appropriate.

The fluctuating mass flux component, $(\rho u)'$, $(\rho v)'$, and $(\rho w)'$, turbulence intensities were combined into a compressible turbulent kinetic energy (see Fig. 7), which was defined as[6]

$$k_c \equiv \frac{\overline{(\rho u)'^2} + \overline{(\rho v)'^2} + \overline{(\rho w)'^2}}{2\bar{\rho}^2} \tag{3}$$

One prominent feature of Fig. 7 was the two peak values of k_c located near $y/d \approx -4.5$ and $z/d \approx \pm 1.5$. Symmetry about the z axis was also observed. The positions of the two peaks coincided with the counter-rotating vortex pair in Fig. 5. The increase in k_c within each vortex was likely the result of an increased production due to the effects of the three-dimensional, mean, dilatational strain rates and to a lesser extent convection, or entrainment, of high turbulence intensity boundary-layer fluid.

Presented in Fig. 8 are the x–y Reynolds shear stress in transformed variables, i.e., all of the terms in Eq. (2). The first term (Fig. 8a) on the right-hand side of Eq. (2) was directly measured. The second term (Fig. 8b) was estimated via the uncoupling procedure. Recall that in the formulation of Eq. (2) it was proposed that for thin layer type flows the second term would be small relative to the first. The validity of this postulate for the present flow is confirmed by comparing the magnitude of the shear stresses in Figs. 8a and 8b, where it can be seen that first term is approximately one order of magnitude larger than the second. The total compressible shear stresses τ_{xy}^T, i.e., the combined results of Figs. 8a and 8b, are shown in Fig. 8c. A prominent feature of the turbulent shear stress distribution was the peak located within the core of the plume. Comparing with the cross-plane velocity vector contour in Fig. 4, it was noticed that the peak in the shear stress was located along the centerline interaction of the two vortices. Increased production due to increased mean bulk compression ($\nabla \cdot V < 0$) and additional x–z and y–z shear-strain rates in the region between the two vortices appears to be the primary reason for this peak in the turbulent shear stress. In addition, the shear stress around the periphery of the plume changed sign near the midspan of the plume ($y/d = -4.0$). Although opposite in sign, the magnitude of the shear stress around the lower or freestream side of the jet was very consistent with that along the upper or top wall side of the jet. The sign of the shear stress around the periphery of the plume is explainable by physical momentum transfer arguments. For example, consider a positive transverse momentum fluctuation on the freestream or lower side of the plume. As the fluid clump is displaced up into the plume from y to $y + \Delta y$, it brings with it an axial momentum that is higher than that at $y + \Delta y$ (the u velocity gradient can be inferred from Fig. 3b), thereby producing a negative turbulent shear stress. The same analysis predicts the positive shear

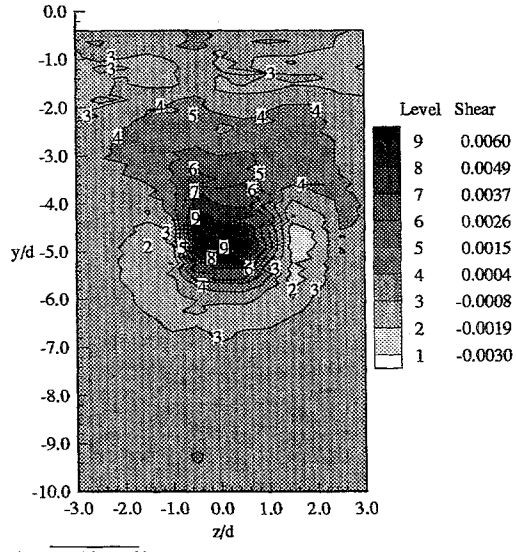

a) $-\overline{(\rho u)'(\rho v)'}/\bar{\rho}$

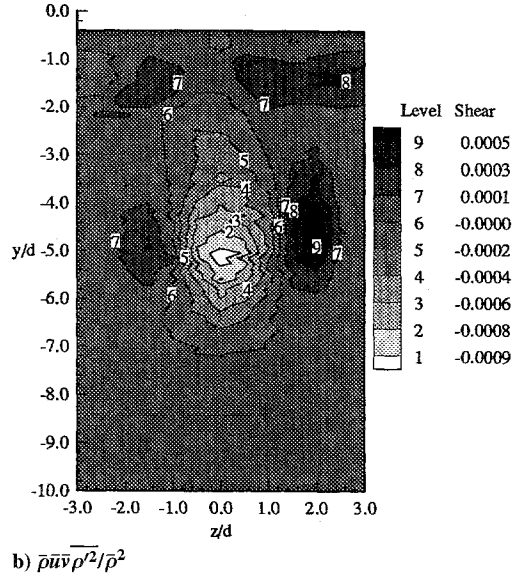

b) $\bar{\rho}\bar{u}\bar{v}\overline{\rho'^2}/\bar{\rho}^2$

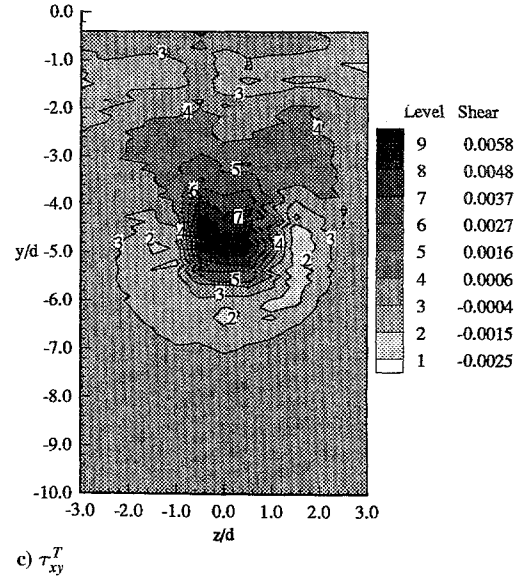

c) τ_{xy}^T

Fig. 8 x–y cross-wire shear stresses/$\bar{\rho}\bar{u}^2$($\times 10^3$, x/d = 40).

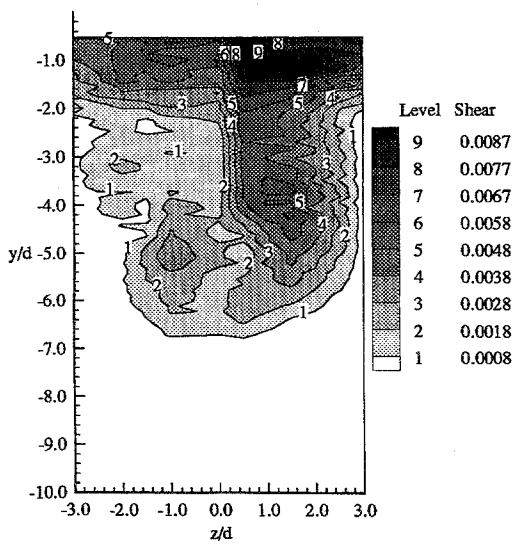

Fig. 9 x–z **cross-wire shear stress,** $\tau_{xz}^T/\bar{\rho}\bar{u}^2(\times 10^3, x/d = 40)$.

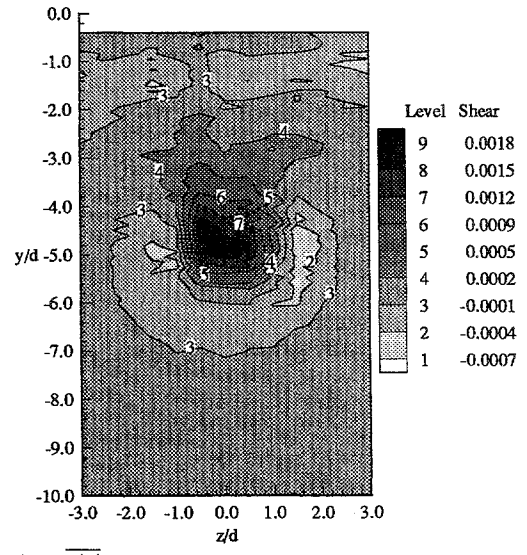

a) $-\bar{\rho}\overline{u'v'}$

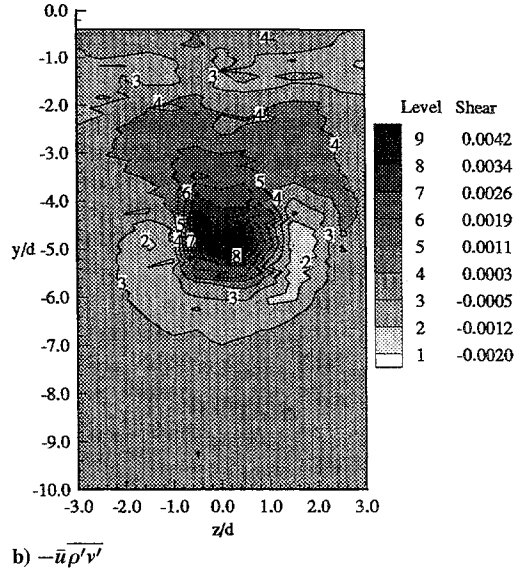

b) $-\bar{u}\overline{\rho'v'}$

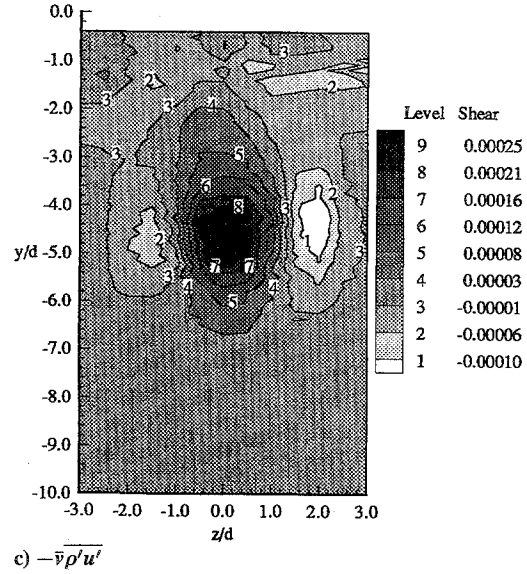

c) $-\bar{v}\overline{\rho'u'}$

Fig. 10 x–y **Reynolds shear stresses** $/\bar{\rho}\bar{u}^2(\times 10^3, x/d = 40)$.

on the top or boundary-layer side of the plume. Finally, as with the k_c, symmetry about the z axis was also observed in Fig. 8.

Given in Fig. 9 are the x–z transformed Reynolds shear stress. Although not shown, the first term on the right-hand side of Eq. (2) was again much larger than the second term. One very interesting facet of the x–z shear stress contour is that it was asymmetrical about the z axis, and the magnitude was positive across the entire plume. This may be explained via the physical momentum arguments described earlier coupled with the vortex interaction effects. Based on the momentum transfer arguments, the shear stress on the left or negative z side of the plume would be less than zero, and the shear stress on the right-hand side would be positive. However, referring to Fig. 9, it is clear that the shear stress on the left-hand side is positive. This apparent discrepancy is explained by including in the argument the secondary flow. A second very distinguishing feature in Fig. 9, which is related to the positive shear stress on the left-hand side of the plume, is the very high shear stress in the boundary layer on the positive z side (i.e., in the region bounded by $z/d \approx 0.0$–3.0 and $y/d \approx -1.7$ to -0.4. This high shear stress was primarily the result of the secondary flow. Recalling the velocity vector contour (Fig. 4), it can be seen that the vortex pair interacts strongly with the wall boundary layer. As mentioned earlier, the merging of the entrained fluid resulted in a stagnation point and the appearance of a third vortex located above the left vortex. Above the right vortex in the boundary-layer region, where the high level of x–z shear stress was observed, the spanwise velocity accelerated from roughly -60.0 m/s ($z/d = 3.0$ and $y/d = -1.0$ to -2.0) nearly 0.0 m/s ($z/d = -1.0$ and $y/d = -1.0$ to -2.0). This represents a locally large z-component, mean, dilatational strain rate. This strain rate also appears in one of the production components of the x–z turbulent shear stress, which could explain the aforementioned peak. In summary then, the positive shear stress in the left-hand side of the plume was most likely the combined result of the increased strain rates due to the vorticity and convection of the turbulent structures generated near the wall. The physical mechanisms responsible for the positive shear stress in the boundary-layer region above the left vortex are analogous to those described for the left-hand vortex (i.e., increased strain rates due to the third vortex, as well as a convection from the right, and increased production due to the z component of the dilatational strain rate). The spanwise velocity gradients just above the left vortex affected the shear stress in that region. For example, the flow from the left that stagnated at $y/d = -2.0$ and $z/d = -1.0$ (see Fig. 4) decelerated from approximately 30 to about 0.0 m/s. Hence, the shear stress production in that region was reduced. The local region of near zero shear at $y/d = -2.2$ and $z/d = -1.2$ (Fig. 9) provides evidence of the reduced production. The relatively high shear stress located at $y/d = -3.2$ and $z/d = -1.8$ was colocated with a local region of spanwise velocity acceleration.

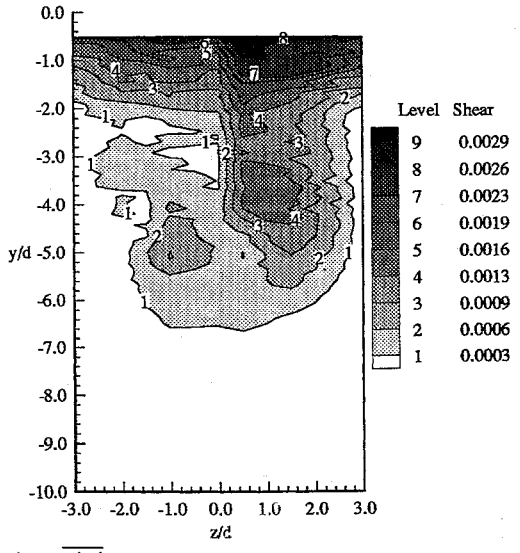

a) $-\bar{\rho}\overline{u'w'}$

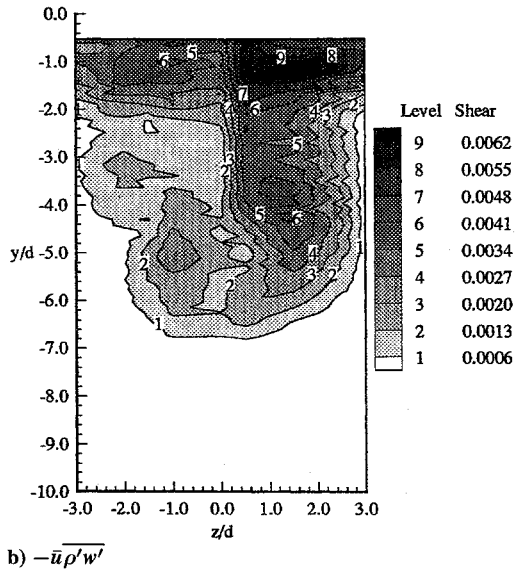

b) $-\bar{u}\overline{\rho'w'}$

Fig. 11 x–z **Reynolds shear stresses** $/\bar{\rho}\bar{u}^2(\times 10^3, x/d = 40)$.

Finally, the right-hand-side, peak shear stress at $y/d = -5.0$ and $z/d = -1.0$, was collocated with the left vortex. This peak was a result of an increased production due to the strain rates generated within the vortex and probably to a lesser extent convection of turbulent structures from the high shear stress region above the right vortex.

Presented in Figs. 10a–10c are the three second-order terms on the right-hand side of the x–y Reynolds shear stress given in Eq. (1). In general, the structures of the contours were very similar to those in Fig. 8. Thus, the conclusions about the interaction between the mean flow and the turbulent shear stress discussed earlier are also applicable to Fig. 10. One striking feature of the results in Fig. 10 is the relative magnitude of the various terms. The first and second terms contributed practically all of the total shear stress (shown in Fig. 8c), where the third term (Fig. 10c) was very small. Interestingly, the present results show that the second term, Fig. 10b, which was mainly due to compressibility, contributed nominally 67.0–75.0% of the total, i.e., the ratio $\bar{u}\overline{\rho'v'}/\bar{\rho}\overline{u'v'}$ was in the range of 2.0–3.0. These results are consistent with the measurements of Bowersox and Schetz,[7] Miller et al.,[17] and Morkovin.[18] Presented in Fig. 11 are the two significant x–z Reynolds shear stresses as given in Eq. (1). As with the x–y results, the structure of the shear stress was similar to those present in the transformed or cross-wire variables (Fig. 9). The results in Fig. 11 indicate that the ratio $\bar{u}\overline{\rho'w'}/\bar{\rho}\overline{u'w'}$ was also in the range of 2.0–3.0.

Conclusions

Detailed, three-dimensional, compressible turbulence and mean flow measurements were acquired across the plume of a low-angled supersonic injection into a supersonic crossflow. The present measurements indicated that the mean and turbulent structure were strongly influenced by two counter-rotating vortices within the core of the injection plume. The turbulent kinetic energy contour was found to have two peak values that were co-located with each vortex. It is suspected that the increased turbulent kinetic energy was a result of increased production due to the effects of the mean, three-dimensional, dilatational strain rates and an entrainment of high turbulence intensity boundary-layer fluid. The overall structure of the turbulent shear stress distribution across the plume was found to be highly three-dimensional and complicated by the presence of additional strain rates caused by the secondary vortex flow and the convection of turbulent structures. Finally, compressibility was found to be very important, accounting for 67.0–75.0% of the total Reynolds shear stress, i.e., the ratios $\bar{u}\overline{\rho'v'}/\bar{\rho}\overline{u'v'}$ and $\bar{u}\overline{\rho'w'}/\bar{\rho}\overline{u'w'}$ were both found to be in the range of 2.0–3.0.

Acknowledgments

The authors thank A. Nejad of the Wright Laboratory and T. Chen of Taitech, Inc., for sponsoring this work.

References

[1]Fuller, E., Mays, R., Thomas, R., and Schetz, J., "Mixing Studies of Helium in Air at High Supersonic Speeds," *AIAA Journal*, Vol. 30, No. 9, 1992, pp. 2234–2243.

[2]Mays, R., Thomas, R., and Schetz, J., "Low Angle Injection into a Supersonic Flow," AIAA Paper 89-2461, July 1989.

[3]Schetz, J., Thomas, R., and Billig, F., "Mixing of Transverse Jets and Wall Jets in Supersonic Flow," *Separated Flows and Jets*, edited by V. V. Koslow and A. V. Dovgal, Springer–Verlag, Berlin, 1991, pp. 807–837.

[4]McClinton, C., "The Effects of Injection Angle on the Interaction Between Sonic Secondary Jets and a Supersonic Free Stream," NASA TN-6669, Feb. 1972.

[5]Papomoschou, D., and Roshko, A., "The Compressible Turbulent Shear Layer: An Experimental Study," *Journal of Fluid Mechanics*, Vol. 197, 1988, pp. 453–477.

[6]Bowersox, R., and Schetz, J., "Compressible Turbulence Measurements in a High-Speed High Reynolds Number Mixing Layer," *AIAA Journal*, Vol. 32, No. 4, 1994, pp. 758–764.

[7]Bowersox, R., "Thermal Anemometry," *Handbook of Fluid Dynamics and Fluid Machinery*, edited by J. Schetz and A. Fuhs, Wiley, New York (to be published).

[8]Volluz, R., *Handbook of Supersonic Aerodynamics, Section 20, Wind Tunnel Instrumentation and Operation*, Vol. 6, Ordance Aerophysics Lab., NAVORD Rept. 1488, Daingerfield, TX, 1961.

[9]Anon., *Hot-Wire/Hot-Film Anemometry Probes and Accessories*, TSI Incorporated, St. Paul, MN, 1989.

[10]Kovasznay, L., "The Hot-Wire Anemometer in Supersonic Flow," *Journal of the Aeronautical Sciences*, Vol. 17, Sept. 1950, pp. 565–584.

[11]Spangenberg, W., "Heat-Loss Characteristics of Hot-Wire Anemometers at Various Densities in Transonic and Supersonic Flow," NACA TN 3381, May 1955.

[12]Kistler, A., "Fluctuation Measurements in a Supersonic Turbulent Boundary Layer," *Physics of Fluids*, Vol. 2, No. 3, 1959, pp. 290–296.

[13]Schetz, J., *Injection and Mixing in Turbulent Flow*, Vol. 68, Progress in Astronautics and Aeronautics, AIAA, New York, 1980.

[14]Abramovich, G., *Theory of Turbulent Jets*, MIT Press, Cambridge, MA, 1963.

[15]Kim., S.-W., and Benson, T., "Fluid Flow in a Row of Jets in Crossflow—A Numerical Study," *AIAA Journal*, Vol. 31, No. 5, 1993, pp. 806–811.

[16]Cox, S., Fuller, R., Schetz, J., and Walters, R., "Vortical Interactions Generated by an Injector Array to Enhance Mixing in Supersonic Flow," AIAA Paper 94-0708, Jan. 1994.

[17]Miller, R., Dotter, J., Bowersox, R., and Buter, T., "Compressible Turbulence Measurements in Supersonic Boundary Layers with Favorable and Adverse Pressure Gradients," *Joint ASME/AIAA Second Symposium on Transitional and Turbulent Compressible Flows*, Fed.-Vol. 224, 1995, pp. 193–200.

[18]Morkovin, M., "Effects of High Acceleration on a Turbulent Supersonic Shear Layer," *Proceedings of the Heat Transfer and Fluid Mechanics Institute*, Vol. 4, 1955, pp. 1–17.